Interplay between Haldane and modified Haldane models in α-T_3 lattice: Band structures, phase diagrams, and edge states

Kok Wai Lee, Pei-Hao Fu,* and Yee Sin Ang†

Science, Mathematics and Technology, Singapore University of Technology and Design, Singapore 487372, Singapore

(Received 12 December 2023; revised 14 April 2024; accepted 7 May 2024; published 3 June 2024)

We study the topological properties of the Haldane and modified Haldane models in α-T_3 lattice. The band structures and phase diagrams of the system are investigated. Individually, each model undergoes a distinct phase transition: (i) the Haldane-only model experiences a topological phase transition from the Chern insulator ($\mathcal{C} = 1$) phase to the higher Chern insulator ($\mathcal{C} = 2$) phase; while (ii) the modified-Haldane-only model experiences a phase transition from the topological metal phase to the higher Chern insulator phase with identical Chern number $\mathcal{C} = 2$, indicating that $\mathcal{C}$ is insufficient to characterize this system because of the indirect band gap. By plotting the Chern number and $\mathcal{C}$ phase diagram, we show that in the presence of both Haldane and modified Haldane models in the α-T_3 lattice, the interplay between the two models manifests three distinct topological phases, namely the $\mathcal{C} = 1$ Chern insulator (CI) phase, $\mathcal{C} = 2$ higher Chern insulator (HCI) phase, and $\mathcal{C} = 2$ topological metal (TM) phase. These results are further supported by the α-T_3 Hall conductance, zigzag, and armchair edge states calculations. This work elucidates the rich phase evolution of the Haldane and modified Haldane models as α varies continuously from 0 to 1 in an α-T_3 model, thus suggesting α-T_3 lattice as a versatile condensed matter platform for studying topological phase transitions.

DOI: 10.1103/PhysRevB.109.235105

I. INTRODUCTION

Nontrivial topological states of matter in two-dimensional (2D) systems [1,2] have garnered enormous research interest since the theoretical prediction of the quantum anomalous Hall insulator (QAHI) by the Haldane model [3] and its later experimental observations [4–11]. QAHIs are also known as Chern insulators (CIs) because their topological phases are defined by an integer called the Chern number, $\mathcal{C}$ [12]. Originally, the QAHIs experimentally observed were only limited to $\mathcal{C} = 1$. Subsequently, QAHIs with $\mathcal{C} \geqslant 2$ were theoretically proposed [13,14] and experimentally realized [15,16]. Such states are termed higher Chern insulators (HCIs).

Recently, it is demonstrated that the modified Haldane model [17] can lead to antichiral edge states, copropagating edge states along the two parallel edges. The antichiral edge states are in stark contrast to the chiral edge states in QAHIs where the edge states are counterpropagating along the two parallel edges. The antichiral edge states are achieved by modifying the Haldane mass term [3] so that it acts as a pseudoscalar potential to break the time-reversal symmetry and shift the energies of the two Dirac points in opposite directions. Alternatively, it has also been shown that the antichiral edge states can be realized via electron-phonon interaction [18,19] and by combining two subsystems based on the original Haldane model with opposite chirality [20]. These edge states must be accompanied by counterpropagating gapless bulk states to ensure an equal number of left- and right-moving modes. As such, they can exist in topological metals (TMs), conducting materials hosting the coexistence of in-gap bulk states and edge states [21]. The AB-stacked bilayer structure of the modified Haldane model is demonstrated theoretically to result in a higher Chern insulator ($\mathcal{C} = \pm 2$) [22]. Various experimental platforms have been proposed [23–27] to realize the antichiral edge states, and have been experimentally observed in a microwave-scale gyromagnetic photonic crystal [28], a topological circuit [29], a 3D layer-stacked photonic metacrystal [30] and a magnetic Weyl photonic crystal [31]. Remarkably, it has also been shown that the optical phase diagram of the modified Haldane model reveals correlations between pseudospin, perfect circular dichroism, and valley polarization, which can be tuned independently by varying the Fermi energy [32].

There is a strong interest in studying topological phases in different lattice structures, such as honeycomb [3,33,34], Lieb [35–39], dice/T_3 [40–46], checkerboard [47], kagome [48–51], honeycomb kagome [52], square [53], diamond [54], and α-T_3 lattices [55,56]. The discovery of new topological phases in various lattices not only enriches the understanding of condensed matter physics, but also fuels potential technological applications [57,58]. The α-T_3 lattice [59] represents a particularly interesting lattice due to two prominent characteristics, namely a dispersionless zero-energy flat band and α-dependent Berry phase, which leads to interesting phenomena, such as super-Klein tunneling [60,61] and unconventional quantum Hall effect [62,63]. The α-T_3 lattice is an extension of the graphene honeycomb lattice. In addition to the honeycomb A and B sites, an additional C site is introduced in the center of each hexagon, which couples to either the A or B sublattice via the coupling strength, αt. Here, α ($0 \leqslant \alpha \leqslant 1$)

*peihao_fu@sutd.edu.sg
†yeesin_ang@sutd.edu.sg

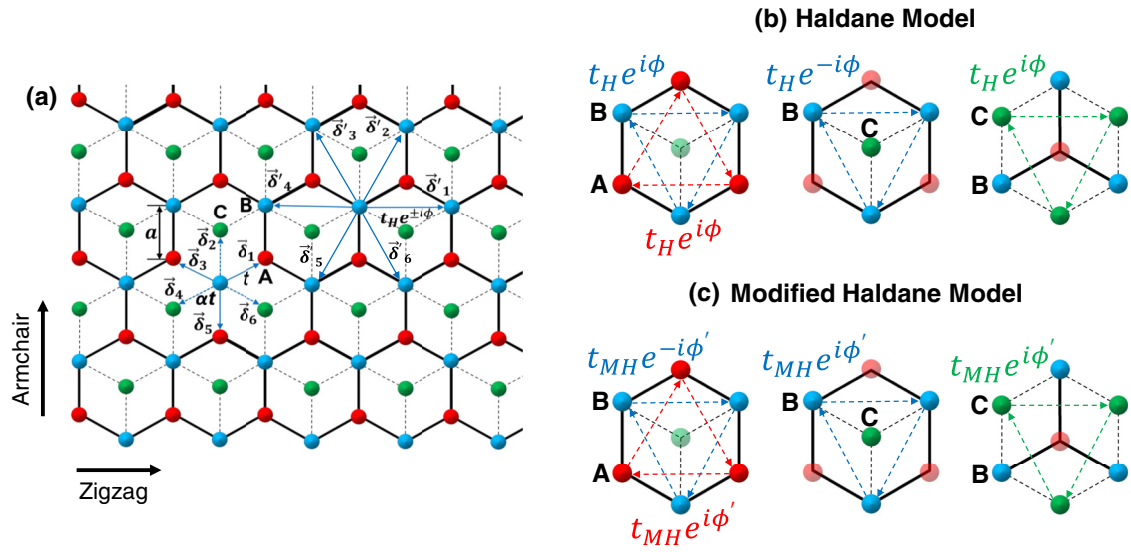

FIG. 1. (a) Schematic of the α-T_3 lattice with zigzag and armchair edges. δ_n and δ'_n ($n = 1, 2, 3, 4, 5, 6$) denote the nearest-neighbor (NN) and next-nearest-neighbor (NNN) vectors pointing from the B sites, respectively, as defined in Table I. Schematic of the (b) Haldane and (c) modified Haldane NNN hoppings. The A, B, and C sites are colored in red, blue, and green respectively.

acts as a tuning parameter and t is the A-B hopping term. As such, the α-T_3 lattice serves as an interpolation between the graphene honeycomb ($\alpha = 0$) and dice/T_3 ($\alpha = 1$) lattices. Its low-energy dispersion consists of a Dirac cone and a dispersionless zero-energy flat band. At a critical doping, $Hg_{1-x}Cd_xTe$ can be mapped onto the α-T_3 lattice with $\alpha = 1/\sqrt{3}$ [64]. α-T_3 lattice can also be realized on optical platforms [59,65]. Various aspects of the α-T_3 lattice have been studied such as electromagnetotransport properties [66–68], thermoelectric properties [69,70], Andreev reflection [71], Josephson effect [71], Floquet engineering [72–78], strain engineering [79], and the effect of Rashba spin-orbit coupling [80].

The Haldane model [3] in a honeycomb lattice gives rise to the Chern insulator phase while in a dice lattice, such model yields higher Chern insulator phases [40,41,81] with $\mathcal{C} = \pm 2$ [40]. The α-T_3 lattice, which interpolates between the honeycomb and dice lattices, provides an interesting system to understand how the Haldane and modified Haldane terms affect the topological phases when α is tuned continuously from the honeycomb limit at $\alpha = 0$ to the dice limit at $\alpha = 1$. How the two models jointly influence the topology of the α-T_3 lattice when α is tuned continuously remains an open question.

In this work, we study the possible topological phases in the α-T_3 lattice that could emerge from the interplay between the Haldane and modified Haldane terms. We first demonstrate the topological properties of the individual cases by determining the Chern number, direct (ΔE_{Direct}), and indirect ($\Delta E_{\text{Indirect}}$) band gaps. We argue that $\mathcal{C}$ is insufficient to characterize the modified Haldane model by showing that $\mathcal{C}$ remains unchanged before and after the system undergoes a phase transition. From the Chern number phase diagram, Hall conductance, and α-T_3 edge states, we show that the interplay between the two models in the α-T_3 lattice manifests three distinct topological phases, namely the $\mathcal{C} = 1$ Chern insulator (CI) phase, $\mathcal{C} = 2$ higher Chern insulator (HCI) phase, and $\mathcal{C} = 2$ topological metal (TM) phase. Our work elucidates the possible phases of the α-T_3 lattice in the presence of the Haldane and modified Haldane terms, and sheds light on the phase evolution of each model as α varies continuously from the honeycomb limit ($\alpha = 0$) to the dice limit ($\alpha = 1$).

The remainder of this paper is organized as follows. In Sec. II, the formulation is presented, which includes the protocols of the Haldane and modified Haldane models in the α-T_3 lattice, topological invariant, and Hall conductance. In Sec. III, the results are presented, which include the bulk band structures, phase diagrams, Hall conductance, and edge states. Lastly, in Sec. IV, this paper is concluded with a brief summary of our results.

II. MODEL AND FORMALISM

A. Model

The α-T_3 lattice with both Haldane and modified Haldane terms as illustrated schematically in Fig. 1 is described by the following Hamiltonian:

$$\mathrm{H} = \mathrm{H}_0 + \mathrm{H}_{\mathrm{H}} + \mathrm{H}_{\mathrm{MH}}, \tag{1}$$

where the first term

$$\mathrm{H}_0 = -\sum_{\langle ij \rangle} t c_i^\dagger c_j - \sum_{\langle jk \rangle} \alpha t c_j^\dagger c_k + \mathrm{H.c.}, \tag{2}$$

describes the nearest-neighbor (NN) hoppings between the B and A (C) sites with strength t (αt). The second and third terms

$$\mathrm{H}_{\mathrm{H}} = \frac{t_{\mathrm{H}}}{3\sqrt{3}} \left[\sum_{\langle\langle ij \rangle\rangle} e^{-i v_{ij} \phi} c_i^\dagger c_j + \alpha \sum_{\langle\langle jk \rangle\rangle} e^{-i v_{jk} \phi} c_j^\dagger c_k \right] + \mathrm{H.c.}, \tag{3}$$

TABLE I. Definitions of the nearest-neighbor (NN) and next-nearest-neighbor (NNN) vectors pointing from the B sites.

NN Vector	Definition	NNN Vector	Definition
δ_1	$\left(\frac{\sqrt{3}}{2}a, \frac{1}{2}a\right)$	δ_1'	$(\sqrt{3}a, 0)$
δ_2	$(0, a)$	δ_2'	$\left(\frac{\sqrt{3}}{2}a, \frac{3}{2}a\right)$
δ_3	$\left(-\frac{\sqrt{3}}{2}a, \frac{1}{2}a\right)$	δ_3'	$\left(-\frac{\sqrt{3}}{2}a, \frac{3}{2}a\right)$
δ_4	$\left(-\frac{\sqrt{3}}{2}a, -\frac{1}{2}a\right)$	δ_4'	$(-\sqrt{3}a, 0)$
δ_5	$(0, -a)$	δ_5'	$\left(-\frac{\sqrt{3}}{2}a, -\frac{3}{2}a\right)$
δ_6	$\left(\frac{\sqrt{3}}{2}a, -\frac{1}{2}a\right)$	δ_6'	$\left(\frac{\sqrt{3}}{2}a, -\frac{3}{2}a\right)$

and

$$\mathrm{H_{MH}} = \frac{t_{\mathrm{MH}}}{3\sqrt{3}}\left[\sum_{\langle\langle ij\rangle\rangle} e^{-i\mu_i v_{ij}\phi'} c_i^\dagger c_j + \alpha \sum_{\langle\langle jk\rangle\rangle} e^{-i\mu_j v_{jk}\phi'} c_j^\dagger c_k\right] + \mathrm{H.c.}, \tag{4}$$

are the Haldane and modified Haldane terms with strengths t_{H} and t_{MH} as well as phases ϕ and ϕ', respectively. Here, $c_i^\dagger$ (c_i) is the spinless fermionic creation (annihilation) operator acting at the ith site, the summation of $\langle ij\rangle$ ($\langle\langle ij\rangle\rangle$) runs over all the nearest (next-nearest)-neighbor sites, $H.c.$ denotes the Hermitian conjugate, $v_{ij} = +1$ (-1) denotes the anticlockwise (clockwise) hopping and $\mu_i = +1$ (-1) denotes the next-nearest-neighbor (NNN) hoppings for A-A or C-C (B-B) sites. The definition of the NN and NNN vectors are shown in Table I.

In contrast to the honeycomb lattice where an electron crosses from one sublattice to the other to hop to an NNN site (e.g., the path undertaken by an electron hopping from a B site to another B site is B-A-B), there are instead two possible paths for an electron to hop from a B site to another B site in the α-T_3 lattice (i.e., B-A-B and B-C-B with hopping strengths t_{H} and αt_{MH}, respectively). All possible Haldane and modified Haldane NNN hopping paths are illustrated in Figs. 1(b) and 1(c), respectively. Here, the B-A-B modified Haldane NNN hopping [blue arrows in the leftmost Fig. 1(c)] is discussed as an example to demonstrate the rules more clearly. Since it is a B-B hopping in a clockwise manner, $v_{ij} = \mu_i = -1$, $t_{\mathrm{MH}}e^{-i\phi'}$ is obtained. Conversely, if it occurs in an anticlockwise manner, then $v_{ij} = +1$ and we obtain $t_{\mathrm{MH}}e^{i\phi'}$ which is the result obtained in Ref. [17].

The resulting k-space Hamiltonian in the sublattice basis, $(|A_k\rangle, |B_k\rangle, |C_k\rangle)^\top$ obtained via the Fourier transformation of Eq. (1) is presented as follows:

$$\hat{\mathrm{H}}(\boldsymbol{k}) = \begin{bmatrix} G_{--} & f^\dagger(\boldsymbol{k}) & 0 \\ f(\boldsymbol{k}) & G_{+-} + \alpha G_{-+} & \alpha f^\dagger(\boldsymbol{k}) \\ 0 & \alpha f(\boldsymbol{k}) & \alpha G_{++} \end{bmatrix}, \tag{5}$$

where

$$f(\boldsymbol{k}) = -t\sum_{n=1,3}^{5} e^{i\boldsymbol{k}\cdot\boldsymbol{\delta}_n}, \tag{6}$$

results from the conventional B-A NN hopping whereas

$$G_{\gamma\beta} = \frac{1}{3\sqrt{3}}[t_{\mathrm{H}} g(\boldsymbol{k}, \gamma\phi) + t_{\mathrm{MH}} g(\boldsymbol{k}, \beta\phi')], \tag{7}$$

$$g(\boldsymbol{k}, \zeta) = \sum_{n=1}^{6} e^{i[(-1)^n\zeta + \boldsymbol{k}\cdot\boldsymbol{\delta}_n']}, \tag{8}$$

results from the Haldane and modified Haldane NNN hopping terms with $\zeta = \phi$ or ϕ', $\boldsymbol{k} = (k_x, k_y)$ and indices $\gamma, \beta = \pm 1$. The competition between the terms shall govern the possible phases of the system, which are revealed directly by the bulk band structure obtained by solving the eigenvalue problem of Eq. (5) numerically.

On the other hand, as to be demonstrated in Sec. II B, the physics around the $\boldsymbol{K}' = (-4\pi/3\sqrt{3}a, 0)$ and $\boldsymbol{K} = (4\pi/3\sqrt{3}a, 0)$ points is also focused on where the states are described by the following Dirac-like Hamiltonian:

$$\mathrm{H}_\eta(\boldsymbol{q}) = \begin{bmatrix} L_{++}^\eta & \tilde{q} & 0 \\ \tilde{q}^\dagger & L_{-+}^\eta + \alpha L_{+-}^\eta & \alpha\tilde{q} \\ 0 & \alpha\tilde{q}^\dagger & \alpha L_{--}^\eta \end{bmatrix}, \tag{9}$$

where $\eta = +1$ (-1) represents the K (K') valley with $\boldsymbol{q} = (q_x, q_y) = \boldsymbol{k} - \boldsymbol{K}$ $(\boldsymbol{k} - \boldsymbol{K}')$, $\tilde{q} = \hbar v_f(\eta q_x - i q_y)$, $\hbar v_f = 3at/2$ and

$$L_{\gamma\beta}^\eta = \frac{t_{\mathrm{H}}}{\sqrt{3}}[-\cos\phi + \eta\sqrt{3}\sin(\gamma\phi)] + \frac{t_{\mathrm{MH}}}{\sqrt{3}}[-\cos\phi' + \eta\sqrt{3}\sin(\beta\phi')], \tag{10}$$

serves as the Dirac mass term determining the bulk spectral gap.

The low-energy dispersion of Eq. (9) can be solved for analytically via the secular equation, $\det[\mathrm{H}_\eta(\boldsymbol{q}) - E_\eta(\boldsymbol{q})] = 0$, which is, however, too complex to be presented in its full form here. For convenience, the three bands and their corresponding wave functions are labeled as $E_m^\eta(\boldsymbol{q})$ and ψ_m^η, respectively. The subscript, $m = -1$, 0, and $+1$ denote the valence, middle, and conduction bands, respectively. For our work, we let $\phi = \phi' = \pi/2$ to ensure the Haldane and modified Haldane NNN hoppings are purely imaginary [40].

At the K' and K points ($\tilde{q} = 0$), Eq. (9) becomes a diagonal matrix. Since a topological phase transition is usually related to a band gap closing-reopening process, we can define both the direct and indirect band gaps of our system in terms of the diagonal elements as follows:

$$\Delta E_{\mathrm{Direct}} = |(L_{-+}^\eta + \alpha L_{+-}^\eta) - \alpha L_{--}^\eta|, \tag{11a}$$

$$\Delta E_{\mathrm{Indirect}} = |(L_{-+}^{+1} + \alpha L_{+-}^{+1}) - \alpha L_{--}^{-1}|. \tag{11b}$$

Equation (11a) and (11b) represents the energy gap between the conduction and valence band edges in the same valley (across different valleys).

B. Topological invariant

Typically, topological phases are associated with topological invariant, which, for our system, is the Chern number, $\mathcal{C}$, which is

$$\mathcal{C} = \mathcal{C}_K + \mathcal{C}_{K'}, \tag{12}$$

where $\mathcal{C}_{K(K')}$ is the so-called valley-dependent Chern number defined as

$$\mathcal{C}_\eta = \frac{1}{2\pi}\iint_{K(K')} \Omega_\eta(\boldsymbol{q})\, d\boldsymbol{q}, \tag{13}$$

with the integration of Berry curvature

$$\Omega_\eta(\boldsymbol{q}) = i\sum_{m=0,1} \frac{\mathrm{Im}\left(\left\langle\psi^\eta_{-1}\middle|v_x\middle|\psi^\eta_m\right\rangle\left\langle\psi^\eta_m\middle|v_y\middle|\psi^\eta_{-1}\right\rangle\right)}{\left(E^\eta_{-1}-E^\eta_m\right)^2}, \tag{14}$$

of the occupied band ($m=-1$) over the vicinity of each valley with $\boldsymbol{v} = \partial \mathrm{H}_\eta(\boldsymbol{q})/\partial\boldsymbol{q}$.

C. Hall conductance

The topological phases indicated by the Chern numbers are revealed in the Hall conductance in the unit of $\sigma_0 = e^2/(2\pi h)$, which is [82,83]:

$$\frac{\sigma_{xy}}{\sigma_0} = \lim_{\epsilon\to 0^+}\sum_{n\neq m}\iint_{\mathrm{BZ}} \frac{(f_{\boldsymbol{k},n}-f_{\boldsymbol{k},m})\mathrm{Im}(\langle\psi_{\boldsymbol{k},n}|\partial_{k_x}\hat{\mathrm{H}}(\boldsymbol{k})|\psi_{\boldsymbol{k},m}\rangle\langle\psi_{\boldsymbol{k},m}|\partial_{k_y}\hat{\mathrm{H}}(\boldsymbol{k})|\psi_{\boldsymbol{k},n}\rangle)}{(E_{\boldsymbol{k},n}-E_{\boldsymbol{k},m})(E_{\boldsymbol{k},n}-E_{\boldsymbol{k},m}+i\epsilon)} dk_x dk_y, \tag{15}$$

where $f_{\boldsymbol{k},n} = \{1+\exp[(E_{\boldsymbol{k},n}-E_F)/(k_BT)]\}^{-1}$ is the Fermi-Dirac distribution of the states with energy $E_{\boldsymbol{k},n}$, Fermi energy E_F at a temperature T. The summation runs over all three bands indexed by $n, m \in \{-1, 0, 1\}$. The integration is performed over the first Brillouin zone (BZ) and $|\psi_{\boldsymbol{k},n}\rangle$ is the nth eigenvector of Hamiltonian $\hat{\mathrm{H}}(\boldsymbol{k})$ given by Eq. (5).

III. RESULTS AND DISCUSSION

Hereafter, the NN hopping strength, t serves as the energy unit ($t=1$) and the phases of the NNN hoppings, ϕ and ϕ' are fixed at $\pi/2$ [40]. Each bulk band structure is plotted along the k_x axis at $k_y = 0$, that is along the path joining the high-symmetry K', M, and K points. The unit of k_x is $k_0 = 4\pi/\sqrt{3}a$ where a is the graphene lattice constant taken to be 1.

A. Bulk spectral and topological properties

By setting the NNN hopping strengths, $(t_{\mathrm{MH}}, t_{\mathrm{H}}) = (0, 0.2)t$ and solving the eigenvalue problem of Eq. (5) numerically, we obtain the Haldane bulk band structure comprising three bands, namely the conduction, middle, and valence bands. Figure 2(a) depicts its evolution with respect to α where it experiences a direct band gap opening-closing-reopening process. At $\alpha = 0$, akin to the graphene case, spectral gaps open at the K' and K points due to the Haldane NNN hopping term, t_{H} but the middle band remains flat owing to the presence of localized electrons at the C sites. The middle band then becomes dispersive when $\alpha \neq 0$ due to the interaction between the B and C sublattices, which causes the spectral gaps to shrink. As the value of α increases, the dispersive nature of the middle band becomes more prominent until it closes the spectral gaps at $\alpha = 0.5$. By further increasing α to 1, the middle band returns to being dispersionless and the spectral gaps are recovered.

The plot of the Chern number, $\mathcal{C}$ and direct band gap, $\Delta E_{\mathrm{Direct}}$ against α is depicted in Fig. 2(b). Here, the blue and red regions represent the $\mathcal{C}=1$ and $\mathcal{C}=2$ topological phases, respectively. Both a jump from $\mathcal{C}=1$ (CI) to $\mathcal{C}=2$ (HCI) and $\Delta E_{\mathrm{Direct}} = 0$ at $\alpha = 0.5$ are observed, indicating that the topological phase transition corresponds to the closing of the direct band gap at $\alpha = 0.5$.

Similarly, by setting $(t_{\mathrm{MH}}, t_{\mathrm{H}}) = (0.2, 0)t$, we obtain the modified Haldane bulk band structure. Figure 2(c) depicts its evolution with respect to α where it experiences an indirect band gap opening-closing-reopening process. At $\alpha = 0$, the bulk band structure is gapless and the band-touching points are shifted vertically in opposite directions due to the presence of the modified Haldane NNN hopping term, t_{MH}. The middle band becomes dispersive and spectral gaps open at the K' and K points when $\alpha \neq 0$ as a result of the interaction between the B and C sublattices. In contrast to the Haldane model, the middle band becomes less dispersive as the value of α increases and it shrinks the indirect spectral gaps until they are closed at $\alpha = 0.5$. Again, the middle band returns to being dispersionless and the spectral gaps are recovered when $\alpha = 1$.

The plot of the Chern number, $\mathcal{C}$ and indirect band gap, $\Delta E_{\mathrm{Indirect}}$ against α is depicted in Fig. 2(d). Unlike the previous case, no jump in the value of $\mathcal{C}$ is observed. Instead, for infinitesimal values of α ($\alpha \to 0$) $\mathcal{C}$ is ill defined due to the gapless spectrum. The sharp increase is not captured perfectly by Fig. 2(d) for want of computational accuracy. As α continues to increase, $\mathcal{C}$ attains a definite value of 2. On the other hand, $\Delta E_{\mathrm{Indirect}}$ indeed becomes zero at $\alpha = 0.5$. Therefore, this system only experiences a phase transition from $\mathcal{C}=2$ (TM) to $\mathcal{C}=2$ (HCI) at $\alpha = 0.5$ as represented by the green and red regions of Fig. 2(d), respectively. Its topology remains unchanged. This shows that the Chern number is insufficient to characterize this particular system. The reason is that when the modified Haldane term is present, it generates valley-dependent shifts to the Dirac cones, therefore there is a local gap and a well-defined Chern number at each valley but there will be no global band gap due to the shifts. Instead, the system now has an indirect band gap. Consequently, for every isoenergy surface, there is at least one band (upper, middle, or lower) involved, which gives the system a metallic feature. The nonzero Chern number for the TM phase ($\alpha < 0.5$) only implies the number of edge states but fails to indicate whether the bulk state is insulating or metallic. The Chern number, $\mathcal{C}$ results presented in Figs. 2(b) and 2(d) agree with those obtained using the full Hamiltonian.

Next, we consider three cases for the combined Haldane models in the α-T_3 lattice: (i) Case I - $t_{\mathrm{H}} > t_{\mathrm{MH}}$, (ii) Case II - $t_{\mathrm{H}} = t_{\mathrm{MH}}$, and (iii) Case III - $t_{\mathrm{H}} < t_{\mathrm{MH}}$ where $(t_{\mathrm{MH}}, t_{\mathrm{H}}) = (0.1, 0.2)t$, $(0.2, 0.2)t$, and $(0.2, 0.1)t$, respectively. They are shown in Figs. 3(a)–3(c) accordingly. In Case I, we obtain the spectral gaps at the K' and K points due to t_{H}, and also their opposite vertical shifts due to t_{MH} as shown in Fig. 3(a) at $\alpha = 0$. Moreover, the presence of t_{MH} leads to the system

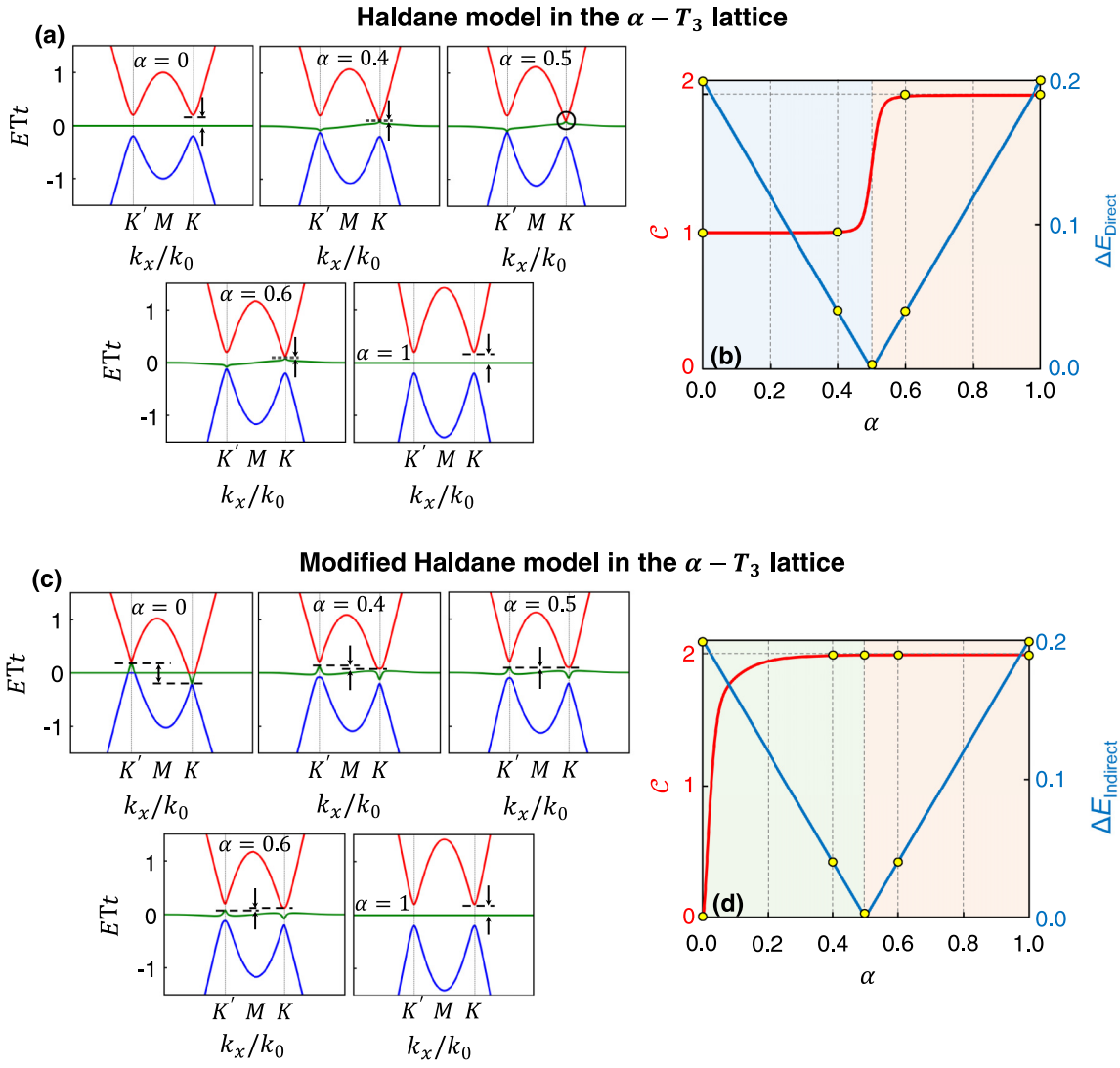

FIG. 2. Evolution of the bulk band structures of the (a) Haldane and (c) modified Haldane models in the α-T_3 lattice with respect to α. The conduction, middle, and valence bands are colored in red, green, and blue, respectively. (b) Chern number, $\mathcal{C}$ and direct band gap, ΔE_{Direct} vs α. (d) Chern number, $\mathcal{C}$ and indirect band gap, $\Delta E_{\text{Indirect}}$ vs α. The yellow dots denote the values of $\mathcal{C}$, ΔE_{Direct} and $\Delta E_{\text{Indirect}}$ at $\alpha = 0$, 0.4, 0.5, 0.6, and 1. For (a) and (b), $(t_{\text{MH}}, t_{\text{H}}) = (0, 0.2)t$ and $\phi = \phi' = \pi/2$. For (c) and (d), $(t_{\text{MH}}, t_{\text{H}}) = (0.2, 0)t$ and $\phi = \phi' = \pi/2$.

experiencing a topological phase transition from $\mathcal{C} = 1$ (CI) to $\mathcal{C} = 2$ (HCI) at $\alpha = 0.25$ instead of 0.5 [Fig. 2(a)]. The opposite manner occurs for Case III. Here, we do not only obtain the shifts at the K' and K points due to t_{MH} but also the spectral gaps due to t_{H} as shown in Fig. 3(c) at $\alpha = 0$. Similarly, the presence of t_{H} causes the system to experience a phase transition from $\mathcal{C} = 2$ (TM) to $\mathcal{C} = 2$ (HCI) at $\alpha = 0.25$ instead of 0.5 [Fig. 2(c)]. On the other hand, as exemplified by Case II [Fig. 3(b)], the system is gapless [remains at $\mathcal{C} = 2$ (HCI)] at $\alpha = 0$ ($\alpha \neq 0$) whenever $t_{\text{H}} = t_{\text{MH}}$. At $\alpha = 1$, Figs. 3(a)–3(c) appear similar, which can be explained by solving the eigenvalue problem of Eq. (9) as follows:

$$\text{H}_{\eta}^{\alpha=1}(\boldsymbol{q}) = \begin{bmatrix} \Delta & \tilde{q} & 0 \\ \tilde{q}^{\dagger} & 0 & \tilde{q} \\ 0 & \tilde{q}^{\dagger} & -\Delta \end{bmatrix}, \tag{16}$$

where $\Delta = \eta(t_{\text{H}} + t_{\text{MH}})$ and the resulting eigenvalues are

$$E_0 = 0; \quad E_{\pm 1}^{\eta} = \pm\sqrt{|\tilde{q}|^2 + \Delta}. \tag{17}$$

The Chern number, $\mathcal{C}$ phase diagram further demonstrates the interplay between t_{H}, t_{MH} and α as depicted in Fig. 4(a) for the specific case of $\alpha = 0.2$. Here, the combined Haldane models in the α-T_3 lattice manifests a total of three phases, namely the $\mathcal{C} = 1$ (CI) phase, $\mathcal{C} = 2$ (HCI) phase, and $\mathcal{C} = 2$ (TM) phase. For instance, at $t_{\text{H}} = 0.2t$, increasing t_{MH} from $0.05t$ to $0.4t$ [going from the left to right in Fig. 4(a)] causes the system to first experience the CI phase, followed by the HCI phase, and finally the TM phase. The CI-HCI and HCI-TM phase boundaries are determined by the closing of the direct and indirect band gaps, respectively. Figure 4(a) exhibits fluctuations at the bottom left region, indicating $\mathcal{C}$ is ill defined due to the system being gapless.

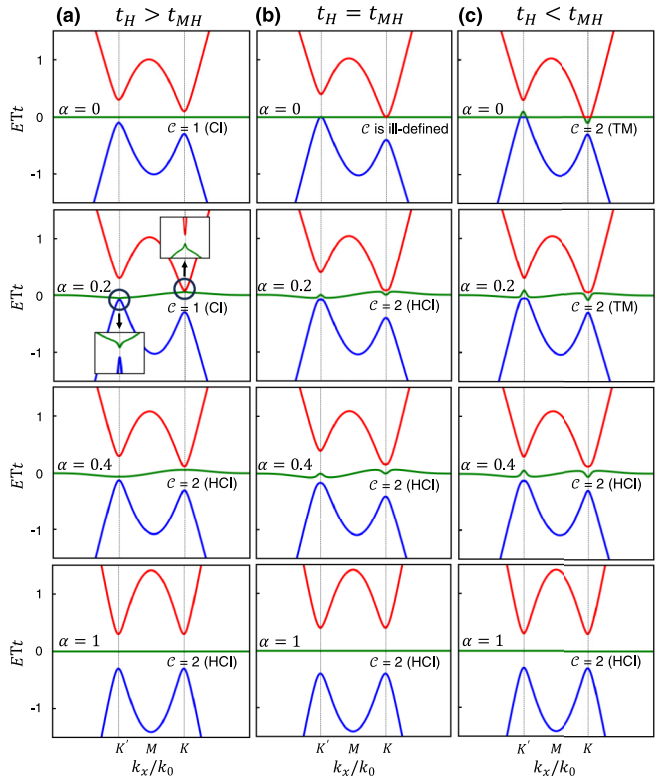

FIG. 3. Evolution of the bulk band structure of the combined Haldane models in the α-T_3 lattice with respect to α for (a) Case I - $t_{\rm H} > t_{\rm MH}$, (b) Case II - $t_{\rm H} = t_{\rm MH}$, and (c) Case III - $t_{\rm H} < t_{\rm MH}$. The values of the parameters are $(t_{\rm MH}, t_{\rm H}) = (0.1, 0.2)t$ for Case I, $(t_{\rm MH}, t_{\rm H}) = (0.2, 0.2)t$ for Case II, $(t_{\rm MH}, t_{\rm H}) = (0.2, 0.1)t$ for Case III, and $\phi = \phi' = \pi/2$ for all three cases. Each panel is labeled with its respective Chern number, $\mathcal{C}$. The conduction, middle, and valence bands are colored in red, green, and blue respectively.

The variation of the CI-HCI and HCI-TM phase boundaries with respect to α is depicted in Fig. 4(b), which satisfy the following relations:

$$t_{\rm H} = \frac{t_{\rm MH}}{1 - 2\alpha}, \tag{18a}$$

$$t_{\rm H} = (1 - 2\alpha) t_{\rm MH}, \tag{18b}$$

respectively. The relations are derived by equating Eqs. (11a) and (11b) to zero. As a result, at $\alpha = 0$, the phase boundaries are degenerate, restoring the graphene case [17]. As α increases, the slopes of the CI-HCI and HCI-TM phase boundaries increases and decreases, respectively, opening the $\mathcal{C} = 2$ HCI phase regime, which eventually dominates the entire phase diagram when $\alpha \geqslant 0.5$.

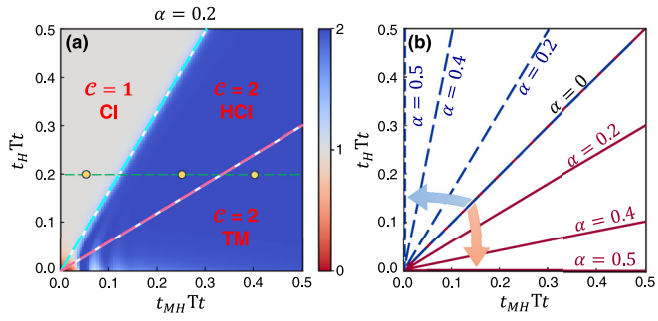

FIG. 4. (a) Chern number, $\mathcal{C}$ phase diagram with respect to $t_{\rm H}$ and $t_{\rm MH}$ at $\alpha = 0.2$ and $\phi = \phi' = \pi/2$. Here, CI, HCI, and TM denote the terms Chern insulator, higher Chern insulator, and topological metal, respectively. The three yellow dots denote the values of $\mathcal{C}$ at $(t_{\rm MH}, t_{\rm H}) = (0.05, 0.2)t$, $(0.25, 0.2)t$, and $(0.4, 0.2)t$. (b) The variation of the CI-HCI (dashed blue) and HCI-TM (solid red) phase boundaries with respect to α for $\alpha = 0$, 0.2, 0.4, and 0.5.

B. Hall conductance

This section relates the topological phases of the system to its Hall conductance. For the CI (HCI) phase with $\mathcal{C} = 1$ (2), σ_{xy}/σ_0 exhibits quantization at 1 (2) when E_F lies within the direct band gap [Figs. 5(a) and 5(b)] corresponding to the width of the conductance plateau. However, there is no quantization of σ_{xy}/σ_0 in the TM phase even if $\mathcal{C} = 2$ because of the in-gap state's quantized conductance in one valley and the bulk states' contribution in the other valley [Fig. 5(c)]. Therefore, the three topological phases are distinguishable by using the Hall conductance within the band gap.

Next, we discuss the effect of temperature on the Hall conductance. Figure 6 depicts the Hall conductance with respect to $t_{\rm MH}$ corresponding to the horizontal line of Fig. 4(a) for various temperatures at $E_F = 0.08t$ and $\alpha = t_{\rm H}/t = 0.2$. At low T (pink curve), σ_{xy}/σ_0 jumps from 1 to 2 at $t_{\rm MH} = 0.12t$, corresponding to the CI-HCI boundary and decays from 2 at around $t_{\rm MH} = 0.33t$, corresponding to the HCI-TM boundary. Therefore, the HCI and TM phases can be distinguished clearly via the respective presence and absence of the quantization at 2. Remarkably, they are only distinguishable at low T. As T increases (green and blue curves), the thermal energy is comparable to the band gap and some of the electrons below the Fermi level are excited into higher bands, thereby reducing the Hall conductance. As a result, the distinctive Hall conductance of the three phases becomes less prominent [84].

C. Edge states

The concept of the bulk-edge correspondence (BEC) states that topological phases possess localized edge states protected by nontrivial bulk topological invariants [85–88]. Therefore, the evolutions of the Chern numbers as well as the phases correspond to that of the edge states of the system.

To plot the zigzag (armchair) edge states, the band structure of the α-T_3 zigzag (armchair) nanoribbon [89,90] is obtained by considering periodic boundary condition along the direction with zigzag (armchair) edges and open boundary condition along the perpendicular direction. The sites along the perpendicular direction are labeled as A_1, B_1, C_1, A_2, B_2, C_2, …, A_N, B_N, C_N, etc. A schematic of the α-T_3 nanoribbon with zigzag and armchair edges is illustrated in Fig. 1(a).

Figure 7 depicts the crossings of the zigzag edge states with the Fermi level. For the case of the Haldane model in the α-T_3 lattice, initially, there is one edge state in each edge propagating in opposite directions [Fig. 7(a)], which is

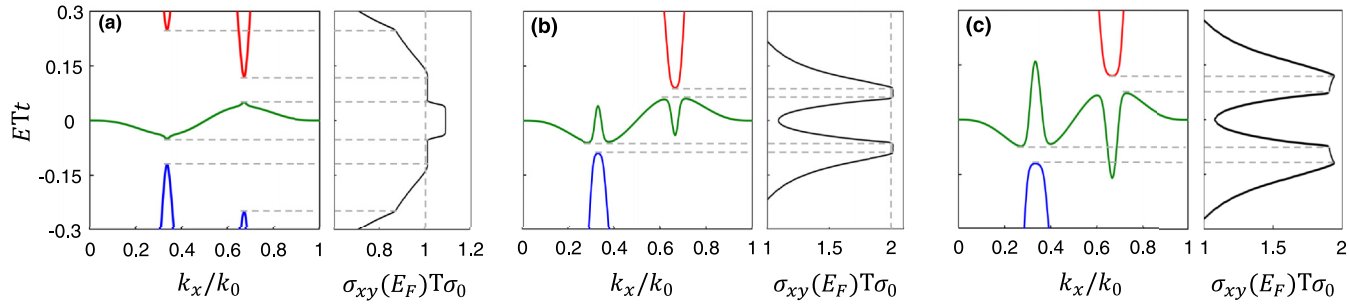

FIG. 5. (a)–(c) Bulk band structures and Hall conductances, which correspond to the three yellow dots in Fig. 4(a). The conduction, middle and valence bands are colored in red, green, and blue, respectively. The thermal energy, k_BT is set at $10^{-6}t$.

consistent with $\mathcal{C} = 1$ (one chiral edge state), signifying the Chern insulator (CI) phase. After the critical point ($\alpha = 0.5$), there are two edge states in each edge propagating in opposite directions [Fig. 7(b)], which is consistent with $\mathcal{C} = 2$ (two chiral edge states), signifying the higher Chern insulator (HCI) phase. For the case of the modified Haldane model in the α-T_3 lattice, before $\alpha = 0.5$, there are two edge states in each edge propagating in opposite directions accompanied by bulk states [Fig. 7(c)]. This coexistence of the in-gap bulk states and edge states satisfies the definition of the topological metal (TM) phase [21]. $\mathcal{C} = 2$ (two chiral edge states) does not encode information regarding the bulk states. After $\alpha = 0.5$, the Fermi level does not cross the bulk states and only the two chiral edge states remain ($\mathcal{C} = 2$) [Fig. 7(d)], indicating the higher Chern insulator (HCI) phase. There are no antichiral edge states in the model concerned in the current work, except for the case when $\alpha = 0$, which is exactly the graphene case demonstrated in Ref. [17]. The reason is that the additional middle quasiflat band couples with the upper and lower bands when $\alpha \neq 0$ and subsequently opens a gap creating additional edge states in the system. Therefore, although the edge states are preserved in the system, the antichirality (copropagating edge states) are destroyed.

Figures 7(e)–7(g) visualize the topological phases manifested by the combined Haldane models as the $\mathcal{C}$ phase diagram of Fig. 4(a) is traversed horizontally to the right. At $(0.05, 0.2)t$, we first obtain one edge state in each edge propagating in opposite directions corresponding to $\mathcal{C} = 1$ (one chiral edge state) [Fig. 7(e)], indicating the CI phase. Next, at $(0.25, 0.2)t$, we obtain two edge states in each edge propagating in opposite directions corresponding to $\mathcal{C} = 2$ (two chiral edge states) [Fig. 7(f)], indicating the HCI phase. Finally, at $(0.4, 0.2)t$, we obtain two chiral edge states ($\mathcal{C} = 2$) and bulk states, indicating the TM phase.

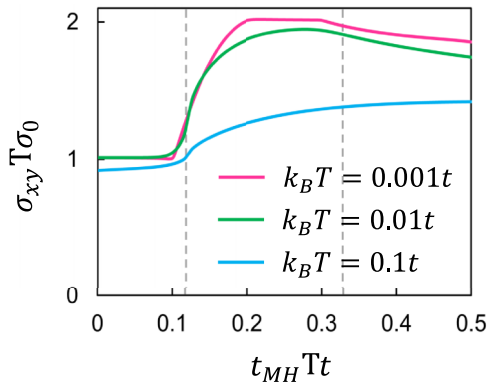

FIG. 6. Hall conductance vs t_{MH} for three values of T. Both values of α and t_{H}/t are fixed at 0.2 whereas E_F is fixed at $0.08t$. The dashed lines indicate the phase boundaries corresponding to Fig. 4(a).

Next, we discuss the zigzag edge state distribution. Figure 8 depicts the probability distributions and localization lengths of the zigzag edge states. Generally, the wave function of the edge states is expected to be in the form of $\exp(-x/\lambda)\cos(bx)$, where b is determined by the Fermi wave number and λ is the localization length [83]. In principle, λ can be numerically extracted via a discrete Fourier transform analysis, which is difficult to achieve. Here, we alternatively approximate the localization length as the minimum number of sites (n_{min}) such that the following condition is satisfied: $(|\psi_{n_{\mathrm{min}}+1}(y)|^2 - |\psi_{n_{\mathrm{min}}}(y)|^2)/|\psi_{n_{\mathrm{min}}}(y)|^2 \times 100\% < 90\%$. Overall, there are two pairs of edges in the TM and HCI phases and one of them has larger localization lengths than the other and the pair in the CI phase, because of the narrower band gap. Additionally, there are also bulk states accompanying the four edge states in the TM phase.

The band structure and edge state distribution of the α-T_3 armchair nanoribbon are presented in Figs. 9 and 10, respectively. For the Haldane model, the Fermi level crosses one (two) chiral edge state(s) before (after) $\alpha = 0.5$, signifying the CI (HCI) phase [Figs. 9(a) and 9(b)]. For the modified Haldane model, when $\alpha < 0.5$, the Fermi level seems to only cross one chiral edge state. This is because the presence of the other chiral edge state and accompanying in-gap bulk states as indicated by the orange and green dots in the center of Fig. 9(c) is shielded from view by the conduction bulk states [Figs. 7(c) and 10(c)]. Nevertheless, the manner of appearance does not affect the overall system topology owing to the bulk-edge correspondence. Hence, Fig. 9(c) still indicates the TM phase. When $\alpha > 0.5$, the Fermi level crosses two chiral edge states [Fig. 9(d)], indicating the HCI phase.

Figures 9(e)–9(g) depict the topological phases manifested by the horizontal line of Fig. 4(a). At $(0.05, 0.2)t$, $(0.25, 0.2)t$, and $(0.4, 0.2)t$, we obtain the CI, HCI, and TM phases respectively [Figs. 9(e), 9(f) and 9(g)].

Similar to the zigzag case, all the edge states are localized differently. However, in contrast to the zigzag case [Figs. 8(c) and 8(g)], the armchair in-gap bulk states and edge states for the TM phase are overlapped [Figs. 10(c) and 10(g)].

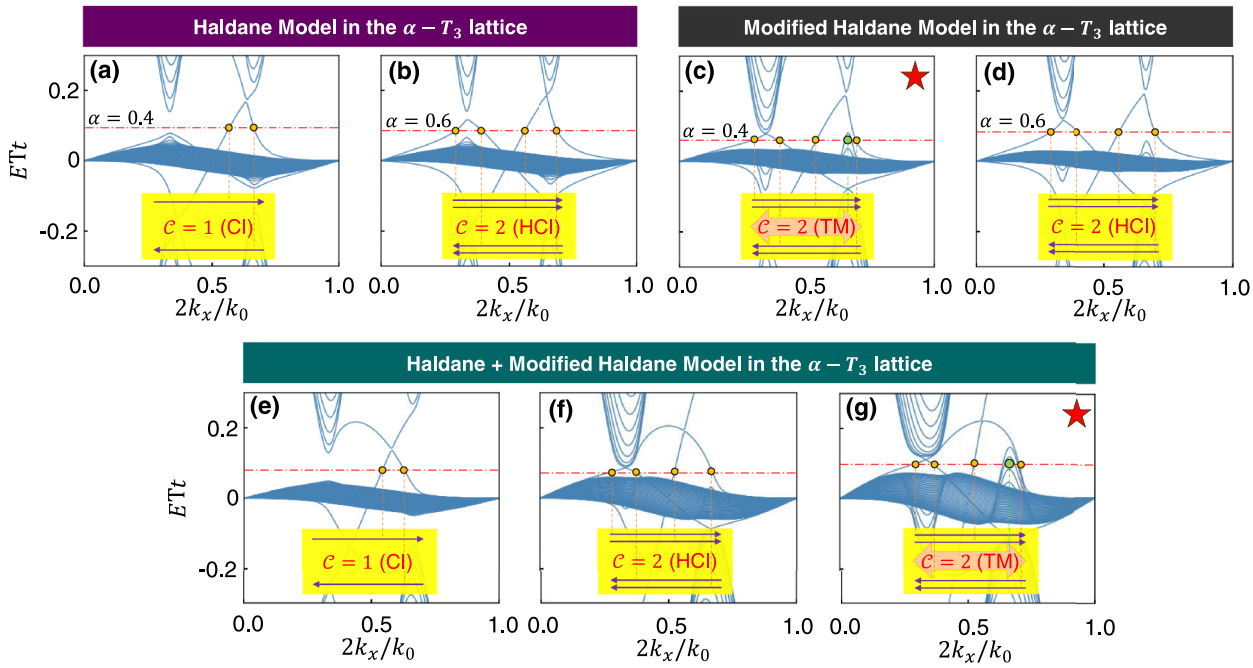

FIG. 7. The band structure of the Haldane model applied to the α-T_3 zigzag nanoribbon at (a) $\alpha = 0.4$ and (b) $\alpha = 0.6$. The values of the parameters are $(t_{\mathrm{MH}}, t_{\mathrm{H}}) = (0, 0.2)t$ and $\phi = \phi' = \pi/2$. The band structure of the modified Haldane model applied to the α-T_3 zigzag nanoribbon at (c) $\alpha = 0.4$ and (d) $\alpha = 0.6$. The values of the parameters are $(t_{\mathrm{MH}}, t_{\mathrm{H}}) = (0.2, 0)t$ and $\phi = \phi' = \pi/2$. (e)–(g) The band structures of the combined Haldane models applied to the α-T_3 zigzag nanoribbon corresponding to the three yellow dots in Fig. 4(a). The zigzag chain contains $N = 50$ AB sites. The star denotes the appearance of the topological metal (TM) phase.

Thus, we conclude that the results related to the bulk properties such as the topological phases and their Chern numbers do not depend on the type of termination chosen for the system (i.e., zigzag and armchair nanoribbons). Based on the Chern numbers and edge states, we demonstrate that in the α-T_3 lattice, the Haldane (modified Haldane) model manifests

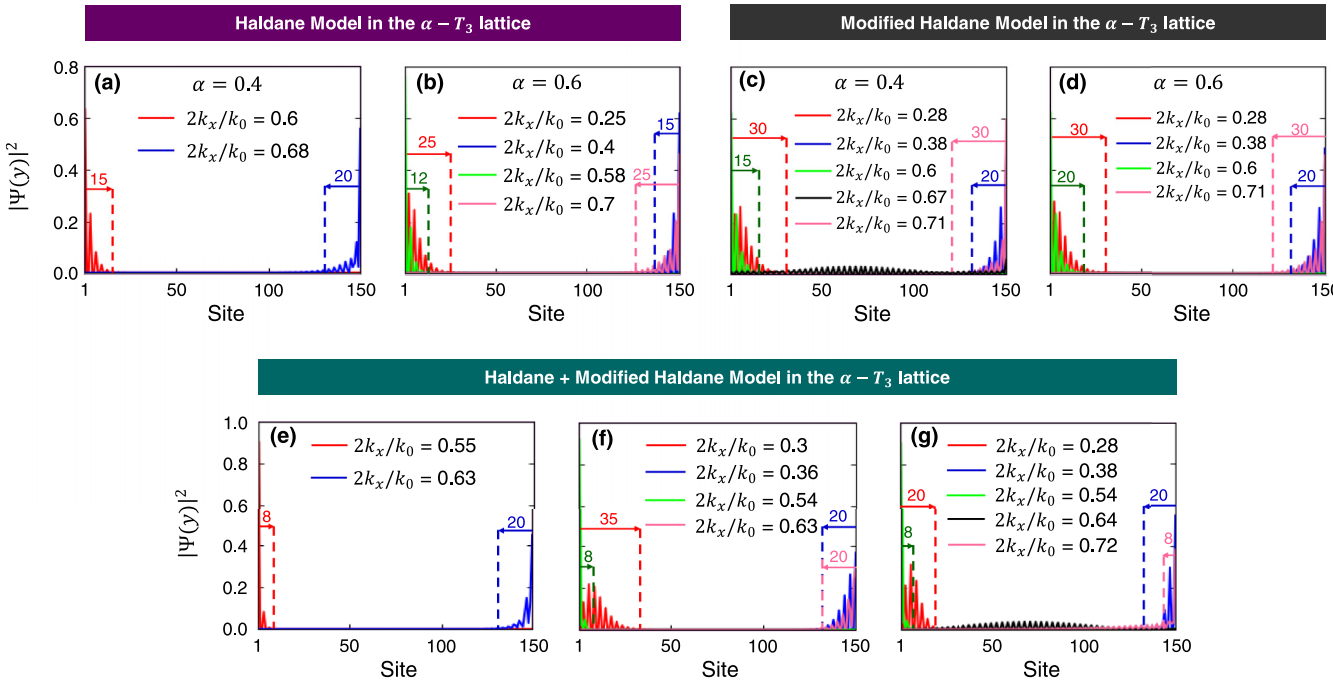

FIG. 8. Probability distributions of the zigzag edge states corresponding to the cases in Fig. 7. The numbers placed on top of the arrows signify the localization lengths of the edge states.

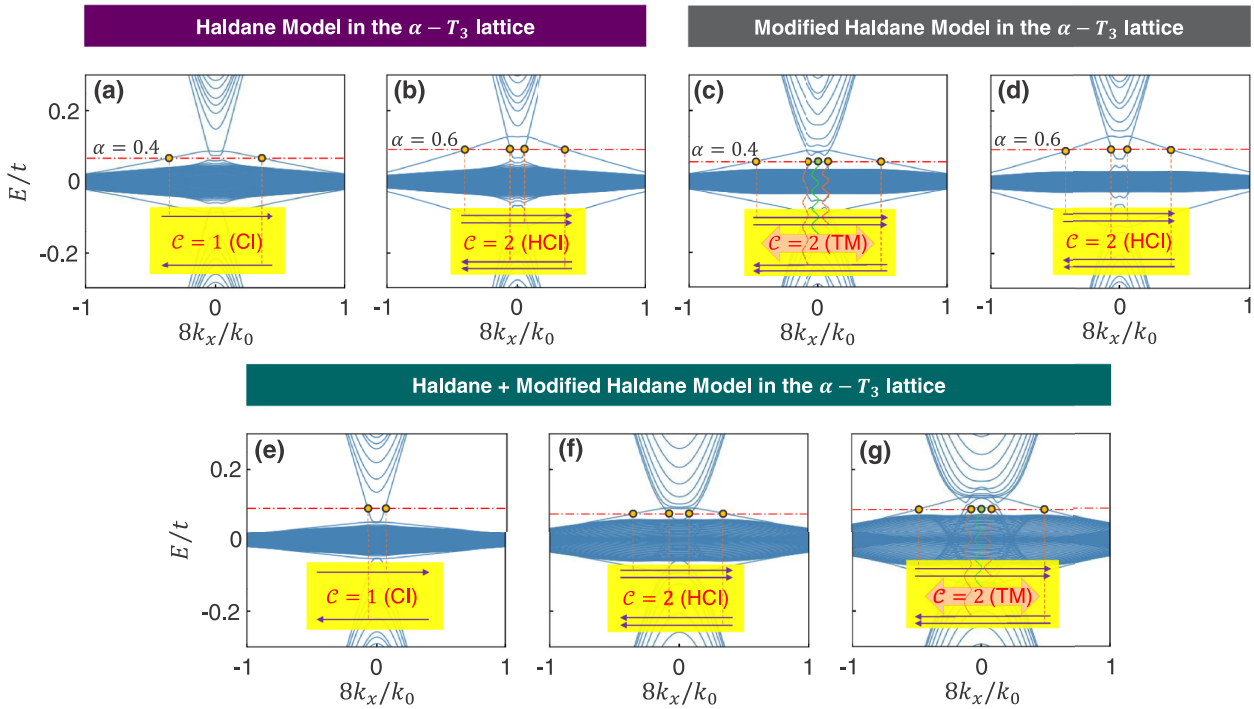

FIG. 9. The band structure of the Haldane model applied to the α-T_3 armchair nanoribbon at (a) $\alpha = 0.4$ and (b) $\alpha = 0.6$. The values of the parameters are $(t_{\rm MH}, t_{\rm H}) = (0, 0.2)t$ and $\phi = \phi' = \pi/2$. The band structure of the modified Haldane model applied to the α-T_3 armchair nanoribbon at (c) $\alpha = 0.4$ and (d) $\alpha = 0.6$. The values of the parameters are $(t_{\rm MH}, t_{\rm H}) = (0.2, 0)t$ and $\phi = \phi' = \pi/2$. (e)–(g) The band structures of the combined Haldane models applied to the α-T_3 armchair nanoribbon corresponding to the three yellow dots in Fig. 4(a). The armchair chain contains $N = 80$ AB sites.

both the CI and HCI (TM and HCI) phases as summarized in Table II accompanied by the honeycomb ($\alpha = 0$) [3,17] and dice ($\alpha = 1$) [41] lattices as specific cases of our phase results.

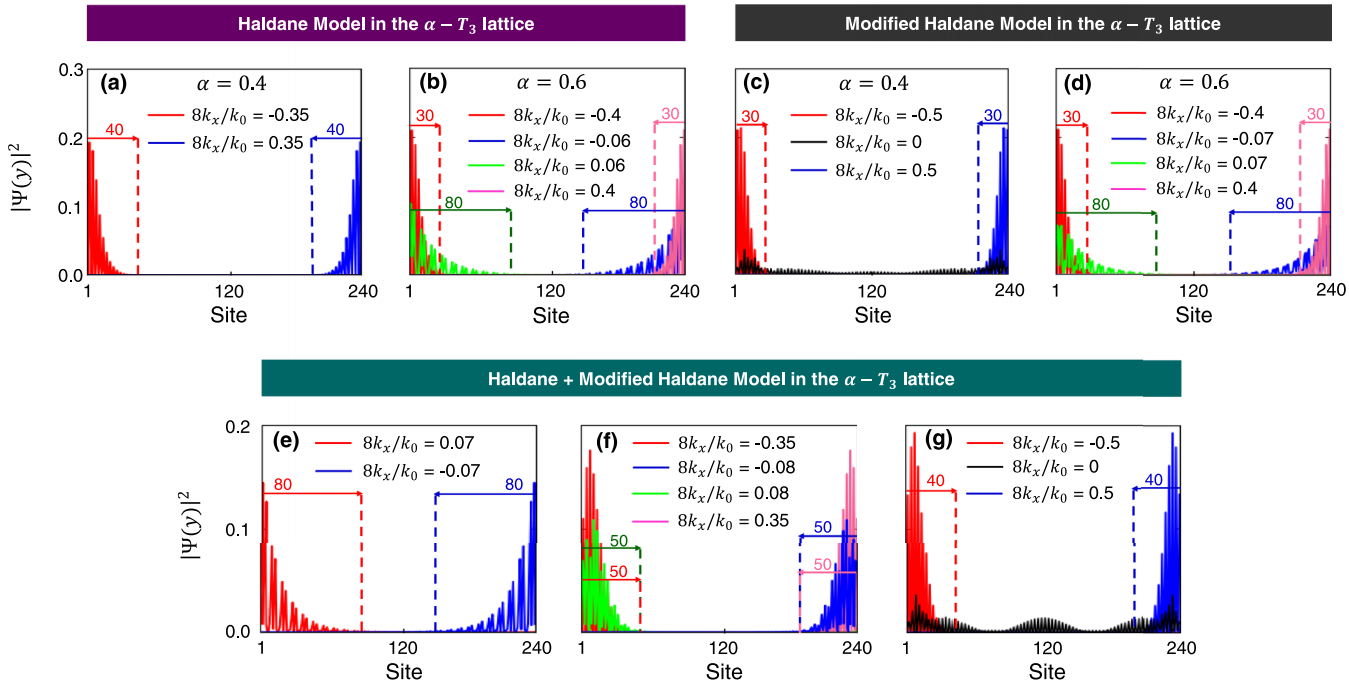

FIG. 10. Probability distributions of the armchair edge states corresponding to the cases in Fig. 9. The numbers placed on top of the arrows signify the localization lengths of the edge states. For (c) and (g), the black-colored probability distribution represents both the bulk and edge states of the topological metal (TM) phase.

TABLE II. Topological phases of Haldane and modified Haldane models in the honeycomb, dice, and α-T_3 lattices.

	Haldane Model		Modified Haldane Model	
Lattice	Phase(s)	Ref(s)	Phase(s)	Ref(s)
Honeycomb	CI	[3]	TM	[17]
Dice	HCI	[40,41]	HCI	Current Work
α-T_3	CI & HCI	Current Work	TM & HCI	Current Work

IV. CONCLUSION

In summary, we study the topological properties of the Haldane and modified Haldane models in the α-T_3 lattice, both individually and collectively. First, we demonstrate that each model manifests a distinct phase transition. The Haldane model experiences a topological phase transition at $\alpha = 0.5$ from the Chern insulator ($\mathcal{C} = 1$) phase to the higher Chern insulator ($\mathcal{C} = 2$) phase. For the modified Haldane model, it experiences a phase transition from the topological metal ($\mathcal{C} = 2$) phase to the higher Chern insulator ($\mathcal{C} = 2$) phase at $\alpha = 0.5$. The fact that $\mathcal{C}$ remains 2 indicates that the Chern number is insufficient to characterize the modified Haldane model. From the Chern number $\mathcal{C}$ phase diagram, we show that the interaction between the Haldane and modified Haldane parameters realizes three distinct topological phases, namely the $\mathcal{C} = 1$ Chern insulator (CI) phase, $\mathcal{C} = 2$ higher Chern insulator (HCI) phase, and $\mathcal{C} = 2$ topological metal (TM) phase. Furthermore, we investigate how the tuning parameter, α influences the phases. At $\alpha = 0$, the system only has the CI and TM phase regimes, which is the graphene case. As α increases, the HCI phase regime is created and dominates the entire phase diagram at $\alpha \geqslant 0.5$. The Chern numbers and phases of the aforementioned cases are supported by calculations of the Hall conductance and edge states. Finally, we remark that we can include more effects into our current model such as the intrinsic [55] and Rashba [80] spin-orbit couplings (SOCs), Floquet engineering [72,74–78,91,92], and strain engineering [79,93] in order to potentially realize new possible topological phases.

ACKNOWLEDGMENTS

This work is supported by the Singapore Ministry of Education (MOE) Academic Research Fund (AcRF) Tier 2 Grant (MOE-T2EP50221-0019).

[1] M. Z. Hasan and C. L. Kane, Rev. Mod. Phys. **82**, 3045 (2010).
[2] X.-L. Qi and S.-C. Zhang, Rev. Mod. Phys. **83**, 1057 (2011).
[3] F. D. M. Haldane, Phys. Rev. Lett. **61**, 2015 (1988).
[4] C.-Z. Chang, J. Zhang, X. Feng, J. Shen, Z. Zhang, M. Guo, K. Li, Y. Ou, P. Wei, L.-L. Wang, Z.-Q. Ji, Y. Feng, S. Ji, X. Chen, J. Jia, X. Dai, Z. Fang, S.-C. Zhang, K. He, Y. Wang *et al.*, Science **340**, 167 (2013).
[5] H.-S. Kim and H.-Y. Kee, npj Quantum Mater. **2**, 20 (2017).
[6] L. B. Shao, S.-L. Zhu, L. Sheng, D. Y. Xing, and Z. D. Wang, Phys. Rev. Lett. **101**, 246810 (2008).
[7] G. Jotzu, M. Messer, R. Desbuquois, M. Lebrat, T. Uehlinger, D. Greif, and T. Esslinger, Nature (London) **515**, 237 (2014).
[8] E. Alba, X. Fernandez-Gonzalvo, J. Mur-Petit, J. K. Pachos, and J. J. Garcia-Ripoll, Phys. Rev. Lett. **107**, 235301 (2011).
[9] M. Serlin, C. L. Tschirhart, H. Polshyn, Y. Zhang, J. Zhu, K. Watanabe, T. Taniguchi, L. Balents, and A. F. Young, Science **367**, 900 (2020).
[10] G. Chen, A. L. Sharpe, E. J. Fox, Y.-H. Zhang, S. Wang, L. Jiang, B. Lyu, H. Li, K. Watanabe, T. Taniguchi, Z. Shi, T. Senthil, D. Goldhaber-Gordon, Y. Zhang, and F. Wang, Nature (London) **579**, 56 (2020).
[11] A. L. Sharpe, E. J. Fox, A. W. Barnard, J. Finney, K. Watanabe, T. Taniguchi, M. A. Kastner, and D. Goldhaber-Gordon, Science **365**, 605 (2019).
[12] D. J. Thouless, M. Kohmoto, M. P. Nightingale, and M. den Nijs, Phys. Rev. Lett. **49**, 405 (1982).
[13] J. Wang, B. Lian, H. Zhang, Y. Xu, and S.-C. Zhang, Phys. Rev. Lett. **111**, 136801 (2013).
[14] C. Fang, M. J. Gilbert, and B. A. Bernevig, Phys. Rev. Lett. **112**, 046801 (2014).
[15] Y.-F. Zhao, R. Zhang, R. Mei, L.-J. Zhou, H. Yi, Y.-Q. Zhang, J. Yu, R. Xiao, K. Wang, N. Samarth, M. H. W. Chan, C.-X. Liu, and C.-Z. Chang, Nature (London) **588**, 419 (2020).
[16] Y.-F. Zhao, R. Zhang, L.-J. Zhou, R. Mei, Z.-J. Yan, M. H. W. Chan, C.-X. Liu, and C.-Z. Chang, Phys. Rev. Lett. **128**, 216801 (2022).
[17] E. Colomés and M. Franz, Phys. Rev. Lett. **120**, 086603 (2018).
[18] J. Medina Dueñas, H. L. Calvo, and L. E. F. Foa Torres, Phys. Rev. Lett. **128**, 066801 (2022).
[19] J. D. Mella, H. L. Calvo, and L. E. F. F. Torres, Nano Lett. **23**, 11013 (2023).
[20] X. Cheng, J. Chen, L. Zhang, L. Xiao, and S. Jia, Phys. Rev. B **104**, L081401 (2021).
[21] W. Cheng, A. Cerjan, S.-Y. Chen, E. Prodan, T. A. Loring, and C. Prodan, Nature Commun. **14**, 3071 (2023).
[22] M. Mannaï, J.-N. Fuchs, F. Piéchon, and S. Haddad, Phys. Rev. B **107**, 045117 (2023).
[23] S. Mandal, R. Ge, and T. C. H. Liew, Phys. Rev. B **99**, 115423 (2019).
[24] C. Wang, L. Zhang, P. Zhang, J. Song, and Y.-X. Li, Phys. Rev. B **101**, 045407 (2020).
[25] M. M. Denner, J. L. Lado, and O. Zilberberg, Phys. Rev. Res. **2**, 043190 (2020).
[26] J. Chen, W. Liang, and Z.-Y. Li, Phys. Rev. B **101**, 214102 (2020).
[27] D. Bhowmick and P. Sengupta, Phys. Rev. B **101**, 195133 (2020).
[28] P. Zhou, G.-G. Liu, Y. Yang, Y.-H. Hu, S. Ma, H. Xue, Q. Wang, L. Deng, and B. Zhang, Phys. Rev. Lett. **125**, 263603 (2020).
[29] Y. Yang, D. Zhu, Z. Hang, and Y. Chong, Sci. China Phys. Mech. Astron. **64**, 257011 (2021).
[30] J.-W. Liu, F.-L. Shi, K. Shen, X.-D. Chen, K. Chen, W.-J. Chen, and J.-W. Dong, Nature Commun. **14**, 2027 (2023).

[31] X. Xi, B. Yan, L. Yang, Y. Meng, Z.-X. Zhu, J.-M. Chen, Z. Wang, P. Zhou, P. P. Shum, Y. Yang *et al.*, Nature Commun. **14**, 1991 (2023).
[32] M. Vila, N. T. Hung, S. Roche, and R. Saito, Phys. Rev. B **99**, 161404(R) (2019).
[33] C. L. Kane and E. J. Mele, Phys. Rev. Lett. **95**, 226801 (2005).
[34] A. Rüegg, J. Wen, and G. A. Fiete, Phys. Rev. B **81**, 205115 (2010).
[35] W.-F. Tsai, C. Fang, H. Yao, and J. Hu, New J. Phys. **17**, 055016 (2015).
[36] N. Goldman, D. F. Urban, and D. Bercioux, Phys. Rev. A **83**, 063601 (2011).
[37] R. Chen and B. Zhou, Phys. Lett. A **381**, 944 (2017).
[38] C. Weeks and M. Franz, Phys. Rev. B **82**, 085310 (2010).
[39] W. Zhu, S. Hou, Y. Long, H. Chen, and J. Ren, Phys. Rev. B **97**, 075310 (2018).
[40] S. Mondal and S. Basu, Phys. Rev. B **107**, 035421 (2023).
[41] B. Dey, P. Kapri, O. Pal, and T. K. Ghosh, Phys. Rev. B **101**, 235406 (2020).
[42] D. O. Oriekhov, E. V. Gorbar, and V. P. Gusynin, Low Temp. Phys. **44**, 1313 (2018).
[43] J. Vidal, R. Mosseri, and B. Douçot, Phys. Rev. Lett. **81**, 5888 (1998).
[44] J. Vidal, P. Butaud, B. Douçot, and R. Mosseri, Phys. Rev. B **64**, 155306 (2001).
[45] E. V. Gorbar, V. P. Gusynin, and D. O. Oriekhov, Phys. Rev. B **103**, 155155 (2021).
[46] D. O. Oriekhov and S. O. Voronov, J. Phys.: Condens. Matter **36**, 125603 (2024).
[47] K. Sun, H. Yao, E. Fradkin, and S. A. Kivelson, Phys. Rev. Lett. **103**, 046811 (2009).
[48] K. Ohgushi, S. Murakami, and N. Nagaosa, Phys. Rev. B **62**, R6065 (2000).
[49] G. Xu, B. Lian, and S.-C. Zhang, Phys. Rev. Lett. **115**, 186802 (2015).
[50] H.-M. Guo and M. Franz, Phys. Rev. B **80**, 113102 (2009).
[51] G. Liu, S.-L. Zhu, S. Jiang, F. Sun, and W. M. Liu, Phys. Rev. A **82**, 053605 (2010).
[52] B. Zhang, F. Deng, X. Chen, X. Lv, and J. Wang, J. Phys.: Condens. Matter **34**, 475702 (2022).
[53] T. D. Stanescu, V. Galitski, and S. Das Sarma, Phys. Rev. A **82**, 013608 (2010).
[54] L. Fu, C. L. Kane, and E. J. Mele, Phys. Rev. Lett. **98**, 106803 (2007).
[55] J. Wang and J.-F. Liu, Phys. Rev. B **103**, 075419 (2021).
[56] O. V. Bugaiko and D. O. Oriekhov, J. Phys.: Condens. Matter **31**, 325501 (2019).
[57] M. J. Gilbert, Commun. Phys. **4**, 70 (2021).
[58] F. Romeo and A. Di Bartolomeo, Nature Commun. **14**, 3709 (2023).
[59] A. Raoux, M. Morigi, J.-N. Fuchs, F. Piéchon, and G. Montambaux, Phys. Rev. Lett. **112**, 026402 (2014).
[60] Y. Betancur-Ocampo, G. Cordourier-Maruri, V. Gupta, and R. de Coss, Phys. Rev. B **96**, 024304 (2017).
[61] E. Illes and E. J. Nicol, Phys. Rev. B **95**, 235432 (2017).
[62] E. Illes, J. P. Carbotte, and E. J. Nicol, Phys. Rev. B **92**, 245410 (2015).
[63] Y. Xu and L.-M. Duan, Phys. Rev. B **96**, 155301 (2017).
[64] J. D. Malcolm and E. J. Nicol, Phys. Rev. B **92**, 035118 (2015).
[65] M. Rizzi, V. Cataudella, and R. Fazio, Phys. Rev. B **73**, 144511 (2006).
[66] F. Li, Q. Zhang, and K. S. Chan, Sci. Rep. **12**, 12987 (2022).
[67] T. Biswas and T. K. Ghosh, J. Phys.: Condens. Matter **28**, 495302 (2016).
[68] S. K. F. Islam and P. Dutta, Phys. Rev. B **96**, 045418 (2017).
[69] X. P. Wen and Z. P. Niu, Phys. Lett. A **489**, 129157 (2023).
[70] M. W. Alam, B. Souayeh, and S. F. Islam, J. Phys.: Condens. Matter **31**, 485303 (2019).
[71] X. Zhou, Phys. Rev. B **104**, 125441 (2021).
[72] B. Dey and T. K. Ghosh, Phys. Rev. B **99**, 205429 (2019).
[73] B. Dey and T. K. Ghosh, Phys. Rev. B **98**, 075422 (2018).
[74] L. Tamang and T. Biswas, Phys. Rev. B **107**, 085408 (2023).
[75] A. Iurov, G. Gumbs, and D. Huang, Phys. Rev. B **99**, 205135 (2019).
[76] A. Iurov, L. Zhemchuzhna, P. Fekete, G. Gumbs, and D. Huang, Phys. Rev. Res. **2**, 043245 (2020).
[77] A. Iurov, L. Zhemchuzhna, G. Gumbs, D. Huang, and P. Fekete, Phys. Rev. B **105**, 115309 (2022).
[78] A. Iurov, L. Zhemchuzhna, D. Dahal, G. Gumbs, and D. Huang, Phys. Rev. B **101**, 035129 (2020).
[79] J. Sun, T. Liu, Y. Du, and H. Guo, Phys. Rev. B **106**, 155417 (2022).
[80] S.-Q. Lin, H. Tan, P.-H. Fu, and J.-F. Liu, iScience **26**, 107546 (2023).
[81] A. Filusch and H. Fehske, Phys. B: Condens. Matter **659**, 414848 (2023).
[82] P.-H. Fu, H.-J. Duan, R.-Q. Wang, and H. Chen, Phys. Lett. A **381**, 3499 (2017).
[83] S.-Q. Shen, *Topological Insulators*, Springer Series in Solid-State Sciences, Vol. 174 (Springer, Berlin, 2012).
[84] X. Ying and A. Kamenev, Phys. Rev. Lett. **121**, 086810 (2018).
[85] Y. Hatsugai, Phys. Rev. Lett. **71**, 3697 (1993).
[86] Y. Hatsugai, Phys. Rev. B **48**, 11851 (1993).
[87] B. I. Halperin, Phys. Rev. B **25**, 2185 (1982).
[88] S. Traverso, M. Sassetti, and N. Traverso Ziani, npj Quantum Mater. **9**, 9 (2024).
[89] M. Fujita, K. Wakabayashi, K. Nakada, and K. Kusakabe, J. Phys. Soc. Jpn. **65**, 1920 (1996).
[90] K. Nakada, M. Fujita, G. Dresselhaus, and M. S. Dresselhaus, Phys. Rev. B **54**, 17954 (1996).
[91] F. Qin, C. H. Lee, and R. Chen, Phys. Rev. B **108**, 075435 (2023).
[92] F. Qin, C. H. Lee, and R. Chen, Phys. Rev. B **106**, 235405 (2022).
[93] M. Mannaï and S. Haddad, J. Phys.: Condens. Matter **32**, 225501 (2020).